

INTERNATIONAL SOCIETY FOR SOIL MECHANICS AND GEOTECHNICAL ENGINEERING



This paper was downloaded from the Online Library of the International Society for Soil Mechanics and Geotechnical Engineering (ISSMGE). The library is available here:

<https://www.issmge.org/publications/online-library>

This is an open-access database that archives thousands of papers published under the Auspices of the ISSMGE and maintained by the Innovation and Development Committee of ISSMGE.

The paper was published in the proceedings of the 7th International Conference on Earthquake Geotechnical Engineering and was edited by Francesco Silvestri, Nicola Moraci and Susanna Antonielli. The conference was held in Rome, Italy, 17 - 20 June 2019.

Keynote Lectures



Taylor & Francis

Taylor & Francis Group

<http://taylorandfrancis.com>

Applications of non-ergodic site response in ground motion modeling

J.P. Stewart & P. Wang

Civil & Environmental Engineering Department, UCLA, Los Angeles, CA, USA

D.P. Teague

ENGEO, Inc., San Ramon, CA, USA

A. Vecchietti

Civil & Mechanical Engineering Department, University of Cassino, Cassino, Italy

ABSTRACT: Site-specific (non-ergodic) seismic hazard analysis is increasingly being employed as part of ground motion hazard characterization for critical projects. Non-ergodic site response can be evaluated from the interpretation of ground motions recorded at (or near) the site or from simulations. The simulation method that is most frequently employed is ground response analysis, which can capture impedance, resonance, and nonlinear effects for vertically propagating shear waves. Such effects are often large contributors to site response, but are not sole contributors, as other effects related to basin geometry can also be influential, particularly at long oscillator periods. We review procedures for conducting ground motion hazard analysis using non-ergodic site response models, including aleatory variability and epistemic uncertainty. We describe preliminary new work related to spatial correlation of site response that is important for some applications. The challenges and benefits of applying these procedures are illustrated through case histories in California, Italy, and Japan

1 INTRODUCTION

By definition, non-ergodic ground motion models (GMMs) provide predictions of the log-normal mean and standard deviation of intensity measures that are customized for the conditions at a particular site. In principle, this can involve adjustment of source, path, and site terms in GMMs to reflect local conditions (the ergodic case involves application of GMMs without such adjustments). As a practical matter, these adjustments are made to ergodic models derived from large (typically global) databases, such as those developed in the Next-Generation Attenuation projects.

In the case of source terms, such adjustments would accommodate knowledge that the energy release on faults in the vicinity of a site of interest is different from that provided in ergodic GMMs. Similarly, adjustments of path terms could be made if certain source-to-site paths are known to have different levels of crustal damping (anelastic attenuation) than is represented in ergodic GMMs. While the concept of non-ergodic path models has been explored for tectonic earthquakes (Landwehr et al. 2016), the use of non-ergodic source and path models is not common for such events. On the other hand, such procedures have been applied for induced seismicity, where the unique characteristics of induced earthquakes require a locally customized approach (e.g., Bommer et al. 2015).

In contrast to the source and path terms, non-ergodic site response has proven to be more achievable in practice, and is increasingly being applied on critical projects (one such project is described in Rodriguez-Marek et al. 2014). From a technical perspective, the benefits of non-ergodic vs ergodic site response ground motion modeling are: (1) a more accurate mean model

and (2) reduced aleatory variability. From a project cost perspective, in many cases site hazard is reduced at long return periods as a result of non-ergodic modeling (mainly due to the reduction in aleatory variability), reducing construction costs.

Here we briefly review non-ergodic procedures and illustrate some issues that have been encountered in recent applications. We describe preliminary investigations of regional correlations of non-ergodic site terms, which begins to address a critical issue for many projects (how proximate does a ground motion instrument need to be to be useful?). We present example case histories that illustrate application of the approach and its potential benefits when implemented in seismic hazard analyses.

2 NON-ERGODIC SITE RESPONSE

2.1 Methodology

Ground motion models generally have four elements,

$$\ln Z_{ij} = F_E(\mathbf{M}_i, F_i) + F_P(\mathbf{M}_i, R_{ij}) + F_S(S_j, x_{IMr,ij}) + \varepsilon \sigma_{ln} \quad (1)$$

where Z_{ij} is a ground motion intensity measure for event i and site j , F_E , F_P , and F_S denote source, path, and site models, respectively, \mathbf{M}_i is the event magnitude, F_i is focal mechanism for event i , R_{ij} is a site-to-source distance for event i and site j , S_j is a vector of one or more site parameters (one of which is typically V_{S30}), $x_{IMr,ij}$ is a reference-site ground motion parameter that is used for nonlinear site response (typically PGA), ε is a random number having a mean of zero and standard deviation of one (standard normal variate), and σ_{ln} is the log-normal aleatory variability (i.e., random variability that remains after the effects of the various independent variables are accounted for through the modeling process, and which is directly accounted for in PSHA; e.g., Bommer and Abrahamson, 2006).

In the non-ergodic site response methodology (Stewart et al. 2017), F_S from the GMM is replaced with a site specific model, typically having the following form,

$$F_S = f_1 + f_2 \ln \left(\frac{x_{IMr} + f_3}{f_3} \right) \quad (2)$$

where f_1 - f_3 are model parameters. Parameter f_1 represents the component of amplification that is independent of the strength of shaking (linear term). Figure 1 shows the shape of the nonlinear term, which illustrates that f_2 represents the slope of site amplification vs $\log(x_{IMr,ij})$ for $x_{IMr,ij} \gg f_3$ and f_3 is a transition ground motion amplitude between linear and nonlinear response.

The f_1 - f_3 model parameters can be derived empirically, if a ground motion instrument with ample recordings is available at or near the site, or through the use of site response

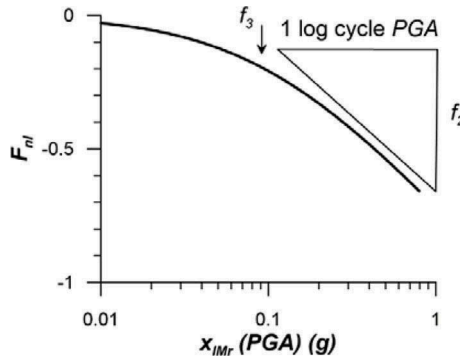


Figure 1. Form of nonlinear site term and illustration of parameters f_2 and f_3 .

simulations. In the empirical approach, a site term (η_S) is developed from the on-site recordings. This involves mixed effects residuals analyses, as described further in Section 3 of this paper. This site term represents the mean misfit of an ergodic model to the data for the site. If the source and path models are regionally unbiased, this mean misfit can be interpreted as being caused by features in the site-specific site response that differ from the ergodic model. The recordings that support the development of η_S are usually of sufficiently low amplitude that nonlinear soil response effects are unlikely to be significant. In this case, model parameter f_1 can be evaluated as,

$$f_1 = \eta_S + f_1^{erg} \quad (3)$$

where f_1^{erg} is the linear site response from the ergodic GMM used in residuals analysis. Parameters f_2 and f_3 are typically derived from simulations assuming one-dimensional wave propagation, as described further in Stewart et al. (2014, 2017) and NCHRP (2012).

The log-normal standard deviation σ_{ln} is often partitioned as,

$$\sigma_{ln} = \sqrt{\tau_{ln}^2 + \phi_{ln}^2} \quad (4)$$

where τ_{ln} represents event-to-event variability and ϕ_{ln} represents within-event variability. Both terms are provided as part of contemporary GMMs. For non-ergodic site response analysis, the components of within-event variability are distinguished,

$$\phi_{ln} = \sqrt{\phi_{ss}^2 + \phi_{S2S}^2} \quad (5)$$

where ϕ_{ss} is the single-station within-event standard deviation (Atkinson, 2006), which includes components of path-to-path variability and event-to-event variability for a given site. Several publications provide period-dependent values of ϕ_{ss} : GeoPentech (2015) provide a model used for several projects in California, while Al Atik (2015) provide such a model for global active tectonic region earthquakes. These models are magnitude-dependent, and Figure 2 compares large- M recommendations to an ergodic ϕ_{ln} model (Boore et al. 2014). Site-to-site standard deviation ϕ_{S2S} represents within-event variability due to variations in site response relative to an ergodic site amplification model. This source of variability vanishes (i.e., $\phi_{ln} = \phi_{ss}$) when a non-ergodic site term is used.

Epistemic uncertainty represents lack of knowledge regarding the most appropriate model to use in some aspect of PSHA (Bommer and Scherbaum, 2008; Bommer, 2012). Ergodic PSHA typically includes alternate source models and alternate GMMs to capture epistemic

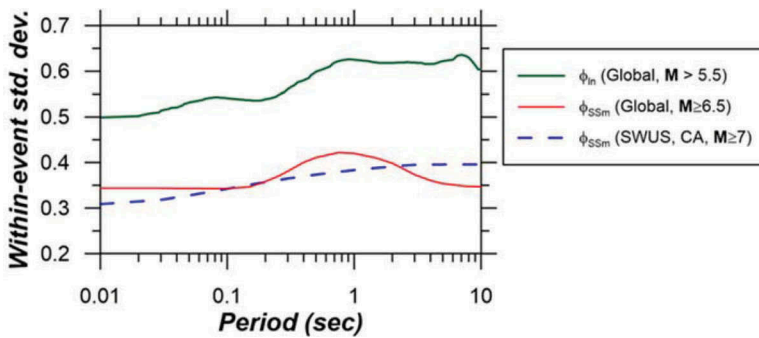


Figure 2. Models for single station and total within-event standard deviation. Global ergodic model from Boore et al. (2014). Global single-station model from Al Atik (2015). California model from South-west US project (GeoPentech, 2015)

uncertainties, according to a logic tree analysis structure. When non-ergodic site response is included, there is additional epistemic uncertainty that can be accounted for with alternate mean amplification and ϕ_{ss} models. Uncertainty in mean site amplification derived empirically can be taken as the standard error of η_S , with potentially additional uncertainty in nonlinear terms due to uncertain dynamic soil properties. Uncertainty in mean site amplification derived from simulations is discussed in Section 2.2.

2.2 Challenges encountered

Non-ergodic site response has increasingly been used on projects where probabilistic seismic hazard analyses (PSHA) are performed. Some challenges associated with application of the procedures summarized in Section 2.1 have been encountered. Challenges associated with non-ergodic analysis the includes ground motion data analysis include:

Challenge 1: Instrument proximity to site. There are occasions where an accelerometer or seismometer is available near, but not at, a site of interest, and that instrument has produced a series of ground motion recordings that could be used in a non-ergodic analysis. The question in such cases is whether non-ergodic site term η_S from one location can be applied in neighboring locations. An example case history where this issue was encountered is described in Section 4.1. The issue is also investigated in Section 3.

Challenge 2: Path and source term errors. When site term η_S is derived from residuals, it captures average site response when the source and path terms used in the residuals are regionally appropriate. This is likely to be the case when a GMM is applied in a region that contributed a large amount of the data employed in its derivation (e.g., coastal California sites and NGA-West2 models). However, this should be routinely checked as part of non-ergodic PSHA, as illustrated in the case history described in Section 4.3.

Challenge 3: Limited data. The derivation of non-ergodic site term η_S becomes more robust as the number of usable recordings from a site increases. For response spectral ordinates, usable recordings are generally from events of $M \geq 4$ (Stafford et al. 2017) and distances within the usable range of the model (400 km for most NGA-West2 models). The case histories described in Sections 4.1-4.3 have different numbers of recordings and variable levels of epistemic uncertainty.

Challenges associated with non-ergodic site response derived from simulations include:

Challenge 4: Epistemic uncertainty when site response derived from simulations. The question in this case is the degree to which wave propagation analyses, using available dynamic soil properties for the site of interest, is able to capture site response. Different approaches have been proposed to address the issue. The two main schools of thought being: (1) the principle source of uncertainty is from incomplete characterization of soil properties (e.g., studies summarized in Figure 7 of Stewart et al., 2017); and (2) both the one-dimensional wave propagation mechanics and the dynamic properties are uncertain (e.g., Chapter 5 of Afshari and Stewart, 2017). This issue is addressed in references, and is not discussed further here.

Challenge 5: Hard rock reference site conditions. Site response is measured relative a reference site condition, which is usually firm to hard rock. For example, the Boore et al. (2014) model uses a reference condition of $V_{S30}=760$ m/s, so non-ergodic site response evaluated using that model will have the same reference condition. When site response is derived from simulations, it is typically referenced to the site condition at the base of the profile. This can create some difficulties when that that reference condition is beyond the range for empirical models. This situation is described in the context of a case history in Section 4.2.

3 SPATIAL CORRELATION OF SITE TERMS

3.1 Database

We began with the NGA-West2 database (Ancheta et al., 2014), which is a global database for active tectonic regions. There is a significant contribution of data from California to the

NGA-west2 database (141 events with $M \geq 4$, 1340 stations, 7975 recordings) over the time period 1938 to 2010. Figure 3 shows the locations of California events. The site portion of the database (Seyhan et al. 2014) was developed to provide the principle site parameters used in model development— V_{S30} and various depth parameters denoted as z_N . These depths indicate the vertical distance from the ground surface to the first crossing of a shear wave velocity iso-surface; the mostly widely used values are $z_{1.0}$ and $z_{2.5}$ for depths to the 1.0 km/s and 2.5 km/s isosurfaces.

As part of this work and other complimentary projects, we have converted the spreadsheet files that comprised the original NGA-West2 flatfile (pertaining to sources, sites, and ground motions) into a formal relational database, which is housed on a local server. Additions of data are made within the relational database. The database is accessed using Python scripts within Jupyter notebooks on DesignSafe (Rathje et al. 2017).

We have identified earthquakes and recordings since 2011 in California, which significantly extend the NGA-West2 database. In this extension of the database, we only consider $M \geq 4$ events, due to difficulties that can be encountered in the analysis of site terms using smaller magnitude data (Stafford et al., 2017). In addition to the NGA-West2 events, Figure 3 also shows the locations of 25 newly added events sorted by magnitude. The 25 newly added earthquakes produced about 8370 three-component recordings within the distance cutoffs suggested by Boore et al. (2014). The data are screened to remove duplicate recordings (e.g., seismometers and accelerometers at the same location) and recordings that appear to be unreliable from instrument malfunctions or similar, which leaves about 4529 usable three-component records.

Figure 4 shows the newly added data in magnitude distance-space in comparison to the NGA-West2 data. The combined data set has 12,504 recordings from 1529 stations and 166 events. The expansion of the data evident in Figure 4 was critical for the present study because our analysis of site terms (defined below) becomes increasingly robust as stations have more

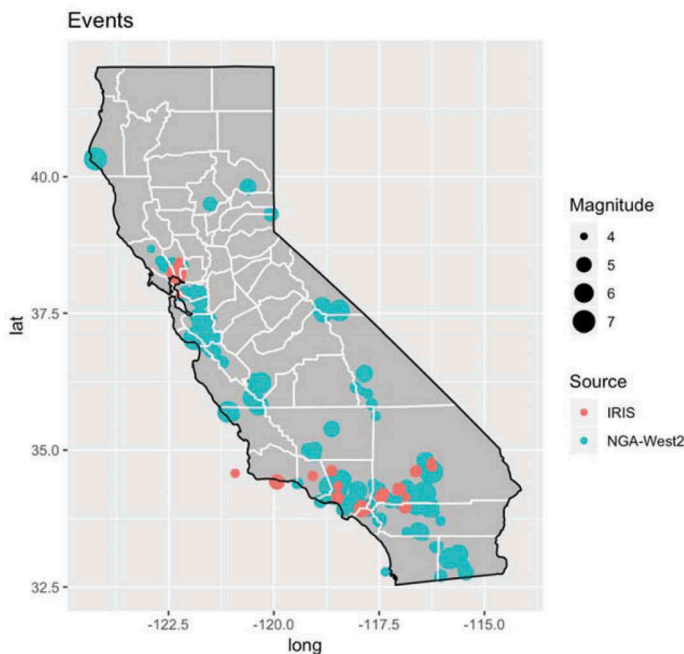


Figure 3. Locations of earthquakes in California and northern Mexico from the NGA-West2 project ($M \geq 4$) and since 2011 ($M \geq 4$) for which ground motion data has been compiled

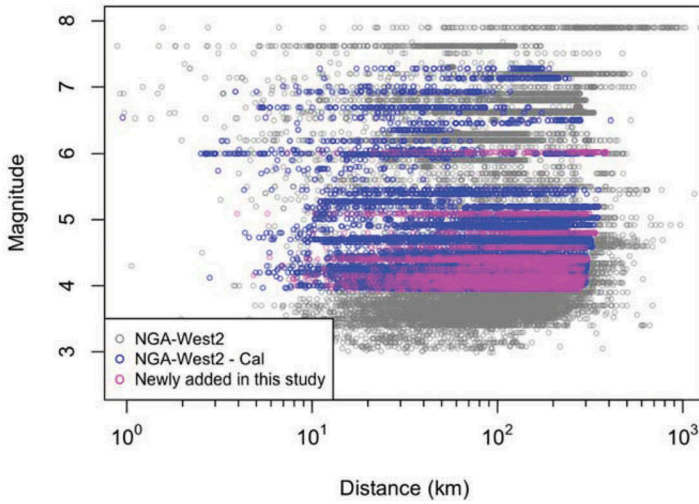


Figure 4. Visualization of databases in magnitude-distance space for NGA-West2 database, the California portion of the NGA-West2 database, and the data newly added in this study for California

usable records. Prior to the present work, there were 267 stations with 10 or more recordings in the study region; whereas the current data set now has 363 such stations.

3.2 Residuals analysis

We use a subset of the NGA-West2 database applicable to events in California region as well as the newly added data developed in the present study, as shown in Figure 4. Using this subset of events, we apply the data screening criteria of Boore et al. (2014). Particularly important elements of those criteria include (1) the use of magnitude and instrument-dependent distance cut-offs that are intended to minimize sampling bias and (2) only using recordings over a range of oscillator periods shorter than $1/f_{hp}$, where f_{hp} is the high-pass frequency selected during component-specific data processing. This frequency is provided in the NGA-West2 flatfile, and was developed in the present work for the added recordings. As shown in Figure 4, the data set spans a magnitude range of about 4 to 7 and a closest distance range of about 1 to 300 km.

The difference between a recorded ground motion and a model prediction is referred to as a residual, R :

$$R_{ij} = \ln(Z_{ij}) - \mu_{\ln}(\mathbf{M}_i, F_i, R_{jb,ij}, S_j) \quad (6)$$

where index i refers to an earthquake and index j refers to a particular station that provides a recording. The quantity Z_{ij} is a ground motion observation expressed as an intensity measure. The term μ_{\ln} is the mean prediction in natural log units of a ground motion model, which uses the arguments in the parenthesis in Eq. (6). We use the Boore et al. (2014) model, which has the arguments listed in Eq. (6), where F is a style of faulting parameter (reverse, strike-slip, etc.), R_{jb} is the Joyner-Boore distance, and other parameters are as defined previously.

We partition the total residuals into systematic effects related the source and site, which are referred to as event terms and site terms, η_E and η_S , respectively. The total residuals are partitioned as,

$$R_{ij} = \delta W_{ij} + \eta_{E,i} \quad (7)$$

where δW_{ij} is a within-event residual, which is further partitioned as,

$$\delta W_{ij} = \eta_{S,j} + \varepsilon_{ij} \quad (8)$$

where ε_{ij} is the remaining residual after systematic effects from source and path have been removed. The spatial correlation analyses described in the next section use the η_S terms. Figure 5 shows the distribution of ground motion stations used in the analysis. Most of the closely spaced records are in the Los Angeles, Imperial Valley, and San Francisco Bay regions of the state.

3.3 Preliminary results

For all possible combinations of stations, we compute the horizontal separation distance between stations, h . We bin the data into equally spaced bins of h that are 0.5 km in width from 0 to 100 km (200 bins in total). For each bin, we compute the variance of the pairs of site terms, which by convention is divided by two to obtain semi-variance, $\gamma(h)$ (Cressie, 1993; Cressie and Wikle, 2011). Figure 6 plots the semivariance for PGA with separation distance, along with a spherical model fit to the data using the gstat package in R (Pebesma, 2004; Graler et al., 2016),

$$\gamma(h) = \begin{cases} c_0 + c_1 \left(1.5 \frac{h}{a} - 0.5 \left(\frac{h}{a} \right)^3 \right), & 0 \leq h < a \\ c_0 + c_1, & h \geq a \end{cases} \quad (9)$$

Parameter c_0 is the *nugget*, which is the value of semivariance at $h=0$. Parameter c_1 is the partial sill, and represents the amount additive to the nugget to reach the horizontal plateau

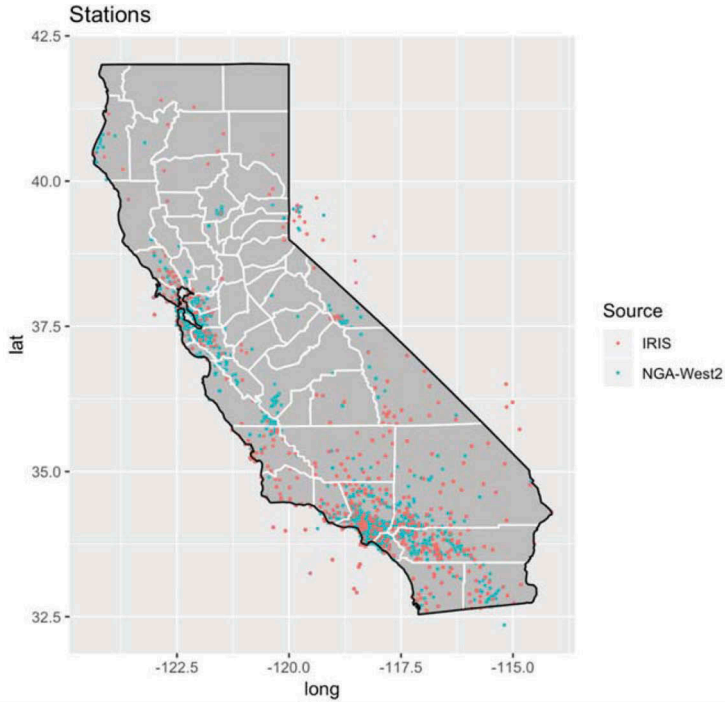


Figure 5. Locations of stations in California from the NGA-West2 project ($M \geq 4$) and since 2011 ($M \geq 4$) for which ground motion data has been compiled

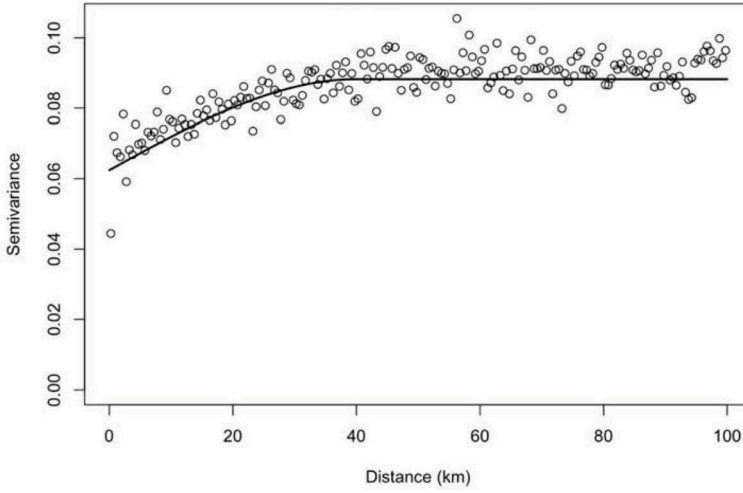


Figure 6. Semi-variance data and fit for non-ergodic site terms of California data.

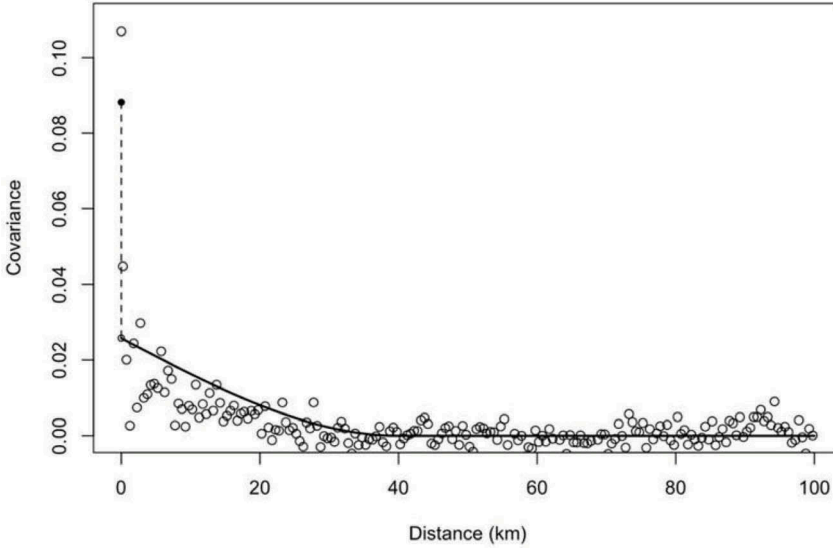


Figure 7. Covariance data and fit for non-ergodic site terms of California data.

of constant semivariance. Parameter α is the range, which indicates the separation distance where semivariance saturates to the value at the plateau. In Figure 6, $c_0 = 0.0624$, $c_1 = 0.0258$, and $\alpha = 40.0$ km. The value of semivariance for $h > \alpha$ corresponds approximately to the square of site-to-site standard deviation, ϕ_{S2S} . The plateau in Figure 6 is 0.0882, which provides $\phi_{S2S} = 0.30$, which is compatible with the values shown in Figure 2.

The same separation distance bins used to compute semivariance are also used to compute covariance, the physical meaning of which is described subsequently. The covariance points are shown in Figure 7 along with a fit that can be derived from that used for the semi-variance. Adopting known relations between semivariance and covariance, $c(0) = c_0 + c_1$ and $c(h) = c(0) - \gamma(h)$ (Cressie, 1993; Cressie and Wikle, 2011), we have,

$$c(h) = \begin{cases} c_0 + c_1, & h = 0 \\ c_1 \left(1 - 1.5 \frac{h}{a} + 0.5 \left(\frac{h}{a} \right)^3 \right), & 0 \leq h < a \\ 0, & h \geq a \end{cases} \quad (10)$$

The function from Eq. (10) is shown in Figure 7. The physical meaning of covariance is related to correlation coefficient. Loosely, correlation coefficient is $c(h)/(c_0 + c_1)$. The trend in Figure 7 shows increasing correlation with decreasing h , as expected. The maximum covariance (for the 0-0.5 km bin) is approximately 0.045, which provides an approximate correlation coefficient of 0.5. It is likely that this correlation can be improved by applying further constraints on the data, for example by controlling for site condition. This has not been considered in the present work.

4 APPLICATIONS

4.1 Lucas Museum

The Lucas Museum of Narrative Art (LMNA) is an approximately \$1.5 billion structure that will be used to house an extensive art collection. The structure, which is currently under construction, was designed by Leslie E. Robertson Associates (LERA). It is seismically-isolated using a system that consists of triple-friction pendulum bearings and cross-rail pendulum bearings. The displacement limit of the seismic isolation system is 1.07 m in each direction and the effective isolator period is approximately 4 sec. Site specific seismic hazard analysis was performed with consideration of non-ergodic site effects in an effort to optimize the design of the seismic isolation system and the superstructure. Challenge (1) (Section 2.2) was encountered for the PSHA at this site.

The Lucas site is located in Los Angeles, California, adjacent to the LA Memorial Coliseum as shown in Figure 8. The site is approximately 0.4 km southwest of the USC seismic recording station on the campus of the University of Southern California (NGA-West2 station #100483).

A non-ergodic site response model was developed using both residuals analysis from the USC station and nonlinear simulations of one-dimensional wave propagation to constrain nonlinear terms (ENGEO, 2017). There are data from 32 earthquakes at the USC station in the NGA-West2 database (Ancheta et al. 2014). Issues related to use of data from this station for the Lucas site were the presence of the accelerograph on the foundation of a structure (which affects ground motions as a result of soil-structure interaction) and the 400 m separation distance.

The soil-structure interaction effect was addressed by developing a foundation/free-field transfer function to account for embedment and base slab averaging effects (NIST, 2012). Fourier amplitudes of the recorded motions were computed, which were divided by transfer function ordinates to estimate free-field amplitudes. These amplitudes were combined with the original phase spectra, new time series were computed, and response spectral ordinates were computed from the time series. Figure 9 shows within-event residuals for the 32 earthquakes along with the mean of residuals (taken as η_S) and its 95% confidence intervals. The confidence intervals in Figure 9 represent the epistemic uncertainty in η_S , and effectively of the site response. While the ergodic models over-predict the site response at short periods, for periods longer than 3 sec η_S is practically zero, indicating lack of bias in the ergodic model.

At the time the Lucas site PSHA was performed, studies of the spatial correlation of non-ergodic site terms (Section 3) had not been performed. Our intuition was that the site response for the USC and Lucas sites would be well correlated, but sought to justify applying the η_S values in Figure 9 to the Lucas site by examining the similarity of site conditions. Figure 10 shows shear wave velocity (V_S) profiles and horizontal-to-vertical (H/V) spectral ratios (from microtremors) at both locations. V_S profiles at the Lucas site were developed using both PS suspension logging and surface wave testing (both MASW and microtremor array methods).

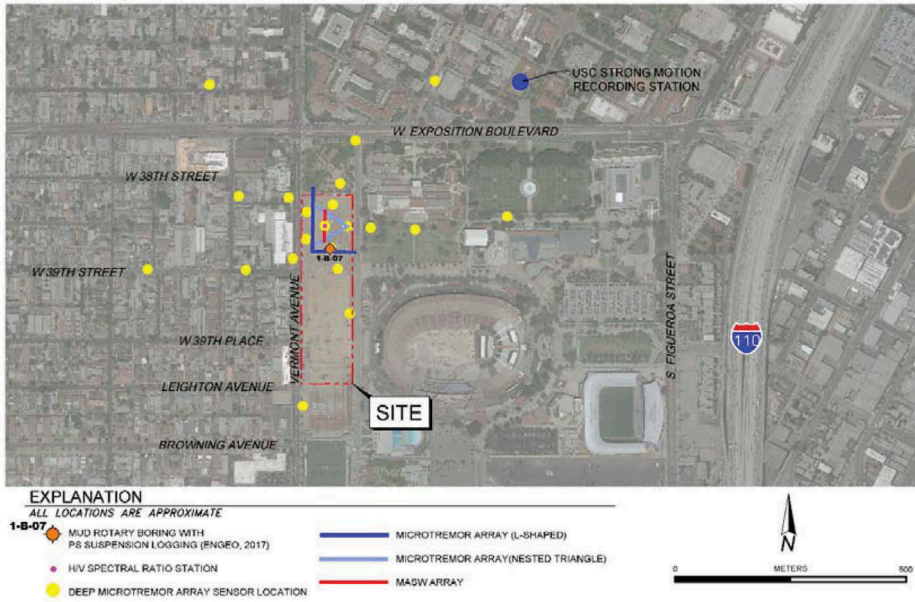


Figure 8. Plan view of the Lucas Museum of Narrative Art project site. Shear wave velocity profiles were developed at the LMNA site using PS suspension logging and surface wave testing (MAW and microtremor array methods). Also shown is the location of the USC station.

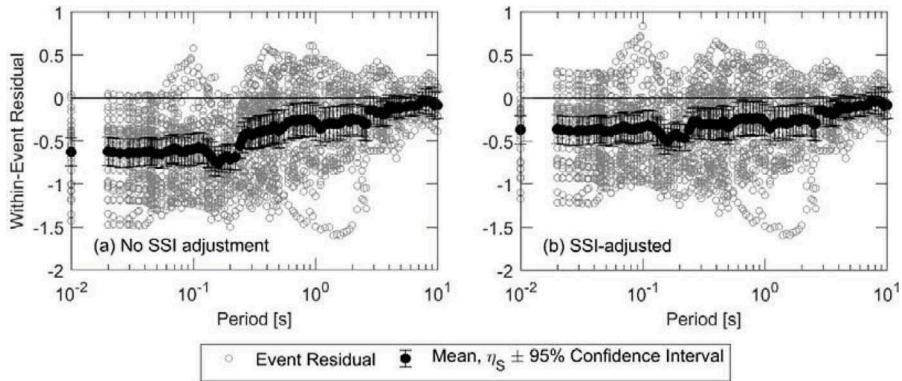


Figure 9. Within-event residuals calculated using 32 earthquakes recorded by the USC station (#100483). Within-event residuals are shown (a) with no soil-structure-interaction (SSI) adjustments and (b) after SSI-adjustment. Also shown are the mean and its 95% confidence intervals.

Due to the non-uniqueness of the surface wave inverse problem, the V_S profile developed from surface wave testingshown in Figure 10 is non-unique and alternative interpretations of V_S were also considered in the analysis using the profile randomization procedure with rejection criteria described in Teague et al. (2018). The seismic velocities are slightly different at the USC and Lucas sites (the V_{S30} values are 300 and 340 m/s, respectively), but the H/V spectral ratios are nearly identical. Our interpretation was that these similarities justified application of the η_S values obtained at the USC site at the Lucas site, especially at long periods, which were critical for the structural design.

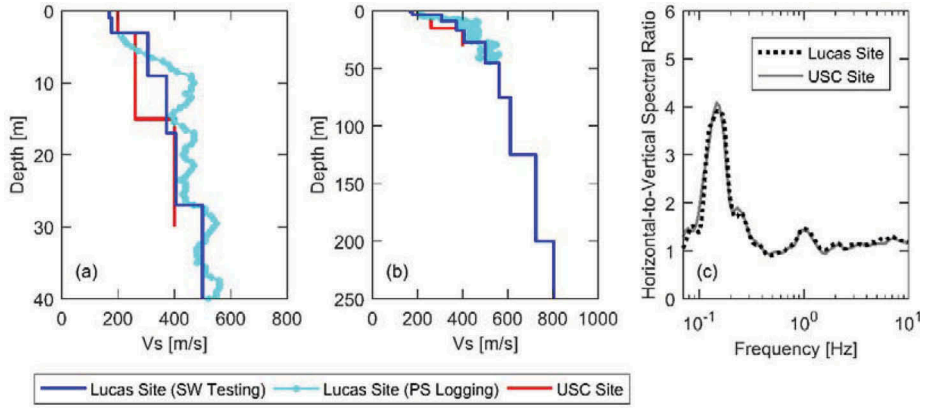


Figure 10. Shear wave velocity profiles developed at the Lucas and USC sites shown to depths of (a) 40 and (b) 250 m. Horizontal-to-vertical spectral ratios from both sites are shown in (c). Lucas site data and H/V spectra for both sites are from ENGEO (2017). USC site V_S profile is from Stewart and Stewart (1997).

The linear site responses at the USC and Lucas sites were somewhat different, due to the different ergodic site responses (from different V_{S30} values). For the Lucas site, we calculated f_l using the USC ground motion records per Eq. (3) and also by performing linear ground response analysis (GRA) simulations. As shown in Figure 11, the f_l values estimated from GRA tended to be higher at periods less than 1.0 sec. Epistemic uncertainties in f_l were considered in the analysis by considering a weighted mean f_l value and upper/lower bounds as indicated by the shaded region in Figure 11. The upper/lower f_l values were taken by adding/subtracting the product of the estimated standard error in f_l at each period (σ_{efl}) and $\sqrt{3}$ to the mean f_l estimate. The range around the mean provided by $\pm\sqrt{3}\sigma_{efl}$ approximates a normal probability density function with a three-point probability mass function (Baker and Cornell, 2003). Using this approach, the results associated with the mean f_l value are assigned a weight of 2/3 and the results associated with the upper/lower f_l values are assigned weights of 1/6. Standard error σ_{efl} was estimated from the available ground motion data for the full range of periods.

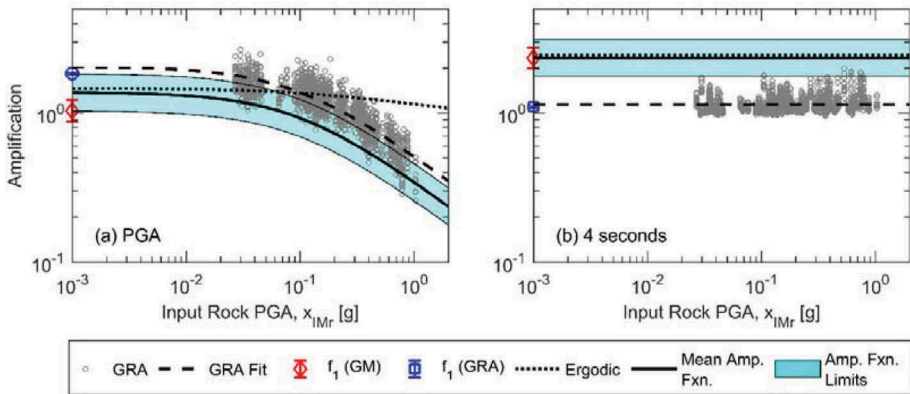


Figure 11. Input/rock PGA versus amplification at the (a) PGA and (b) Sa at 4-sec. Note that the linear f_l parameters calculated from ground motion records at the USC station and linear GRA are shown. The thick solid black line and shaded region represent the mean and limits of the amplification function used in the analysis, respectively.

The nonlinear component of the site term is shown for the site-specific model (derived from simulation) and the ergodic model in Figure 11 for the PGA and S_a at the structure period of 4.0 sec. The site-specific result shows more nonlinearity than the ergodic model at short periods, although both approaches indicate negligible nonlinearity at the long periods of greatest interest for the structural design.

Figure 12 shows the 2475-year return period (i.e., 2% probability of exceedance in 50 years) uniform hazard spectra derived using ergodic and non-ergodic analysis. Epistemic uncertainties in the source model, GMMs, and site response were considered in the analysis, with the results shown in Figure 12 representing the mean hazard. The non-ergodic spectrum is up to 50% lower than the ergodic spectrum at short periods. However, at periods greater than 3 sec, the differences are more modest, with the non-ergodic spectrum about 9% lower than the ergodic spectrum. This reduction comes solely from the reduction in ϕ_{ln} term (refer to Eq. 5) because the mean ergodic and non-ergodic site response were practically identical in this period range. While modest, this reduction at long periods allowed for the use of a more economical seismic isolation system. This system produces lower forces in the superstructure, leading to significant cost savings and architectural benefits.

4.2 Silicon Valley office complex

This project is subject to a non-disclosure agreement that prevents us from revealing the project name and specific location. The site is on the San Francisco Peninsula south of the City of San Francisco, approximately 12 km east of the San Andreas Fault. The site is located at the northwestern end of the Santa Clara Valley in the Coast Ranges geomorphic province of California. The project entails development of a five-story, 74,000 m² steel-frame structure. The first-mode period of the structure is approximately 1.5 sec.

The project site is located 1.4 and 1.0 km from two NGA-West2 ground motion recording stations, which have 21 and 9 low PGA ground motions each, respectively. Due to the non-disclosure agreement, these stations are not identified and are referred to as Stations 1 and 2, respectively. Non-ergodic site response for this site was performed in a similar manner as for the Lucas site, considering both residuals analysis of data from the two stations and GRA simulations to constrain nonlinear terms. Challenges (1), (3), and (5) (Section 2.2) were encountered for the PSHA at this site.

Figures 13a and 13b shows shear wave velocity profiles developed from a joint inversion of surface wave data and H/V spectral ratios from the project site (García-Jerez et al., 2016; Teague et al., 2017 and 2018). V_S profiles were not available at the ground motion stations; however, H/V testing was performed at these locations and the results are shown in Figure 13c. The H/V data from all three locations are similar, with a strong peak occurring

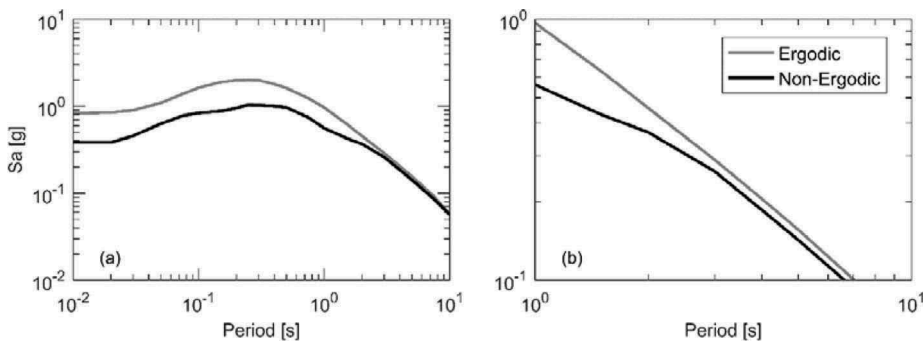


Figure 12. Uniform hazard spectra for a return period of 2475 years (i.e., 2% probability of exceedance in 50 years) derived from ergodic and non-ergodic analysis at the Lucas site, (a) full spectrum, (b) detail of long-period portion of spectrum.

between 0.32 and 0.35 Hz (2.9 to 3.1 sec period). The project site is in a deep basin, with nearby well logs indicating that Franciscan bedrock is at a depth of approximately 0.4 km or greater (Wentworth et al. 2015). The V_S of the Franciscan can vary considerably (less than 0.7 to greater than 2.0 km/s). Due to the non-uniqueness of the inverse problem used to develop the V_S profiles, we could not identify the V_S of this material with certainty and needed to consider this uncertainty in our analysis. The discussion presented here focuses on how the profiles with high bedrock V_S (>2.0 km/s) were considered in the analysis, although profiles with lower bedrock V_S were also considered.

Figure 13c shows the linear, viscoelastic theoretical shear wave transfer functions for the V_S profiles developed from surface wave testing. These theoretical transfer functions generally have fundamental resonant frequencies at or near the peak in the H/V spectra, indicating that they well-represent the estimated fundamental resonant frequency at the site. Given that depths to fast-velocity layers (interpreted as bedrock) are consistent with bedrock depths from nearby well log data (Wentworth et al., 2015) and the transfer function resonant frequencies are consistent with the H/V data, we modelled the full extent of the soil column to rock, rather than truncate the V_S profiles at a shallower depth. Note that the fundamental resonant frequencies associated with some transfer functions are slightly higher than the resonant frequency estimated from the H/V spectra. This is a consequence of how the H/V data were modelled during the inversion used to generate the V_S profiles. While beyond the scope of this paper, some V_S profiles were developed by modelling the H/V data with the diffuse wavefield assumption (García-Jerez et al. 2016) and by consideration of Rayleigh wave ellipticity, which leads to differences in the resulting transfer functions. These alternative strategies for modelling the H/V data represent epistemic uncertainty in the site condition and were considered in the analysis.

As a consequence of the firm base-of-profile site conditions, there is an incompatibility between the site amplification derived empirically (which is relative to a reference site condition of 0.76 km/s) and that derived from simulations (variable reference conditions, but some > 2.0 km/s). This is a common problem, and Stewart et al. (2017) present a solution in which the V_{S30} corresponding to the reference condition at the base of the profile is denoted V_{S30}^B , the ground motion IM for that condition is X^B , and the site amplification relative to that condition is given as:

$$Y^B = \frac{Z}{X^B} \quad (11)$$

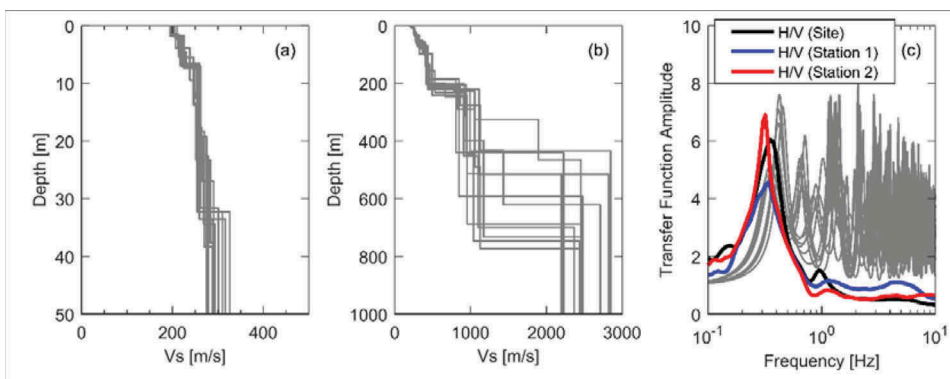


Figure 13. Shear wave velocity profiles developed from surface wave testing shown to depths of (a) 50 and (b) 1000 m and (c) linear, viscoelastic theoretical shear wave transfer functions associated with the V_S profiles in (a) and (b). Also shown in (c) are the experimental H/V data from the project site and from Stations 1 and 2.

where Z is the ground motion IM for the soil site condition (as in Eq. 1). If X is the IM for the reference condition in a GMM (e.g., 0.76 km/s), the amplification relative to that condition (denoted Y) can be related to Y^B as,

$$\ln Y = \ln Y^B + \mu_{\ln Y}(V_{S30}^B) \quad (12)$$

where $\mu_{\ln Y}(V_{S30}^B)$ is the mean site amplification from an ergodic model for the base-of-profile site condition. Eq. (12) can be used to adjust the site amplification derived from simulations (Eq. 11) to be compatible with those derived from empirical data, so that the two estimates can be compared.

The site conditions encountered at the Silicon Valley site did not allow the use of the above procedure, because the $\mu_{\ln Y}(V_{S30}^B)$ term in Eq. (12) is not valid at the site's reference site condition (>2.0 km/s), which is beyond the useable range in the empirical model (i.e., < 1.5 km/s). Accordingly, we considered simulation results (Campbell and Boore 2016), shown in Figure 14, that provide amplification for a 0.76 km/s site condition relative to a very hard rock reference condition of 2.78 km/s (in natural log units, this amplification is denoted F_{760}). Campbell and Boore (2016) provide a range of amplification levels that depend on site kappa and variations in velocity profiles. Some of their results have de-amplification at short periods, which we truncated at unity for the present application. By assuming linear scaling of amplification with $\log V_{S30}$, we define the amplification of 0.76 km/s relative to V_{S30}^B (denoted F_{760}^B) as:

$$F_{760}^B = F_{760} \left(\frac{\ln \frac{0.76}{2.78} + \ln \frac{2.78}{V_{S30}^B}}{\ln \frac{0.76}{2.78}} \right) \quad (13)$$

Figure 14a also shows amplification from ergodic models at their maximum usable velocity (1.5 km/s) for comparison with simulation-based amplification. We used the results in Figure 14a to develop mean and upper/lower bound F_{760}^B values in order to account for epistemic uncertainty as shown in Figure 14b.

The linear term in the site amplification model, referenced to the V_{S30}^B reference condition, can be computed from simulation results in the customary manner (Eq. 11). The corresponding amplification derived from residuals analysis is modified from Eq. (3) as,

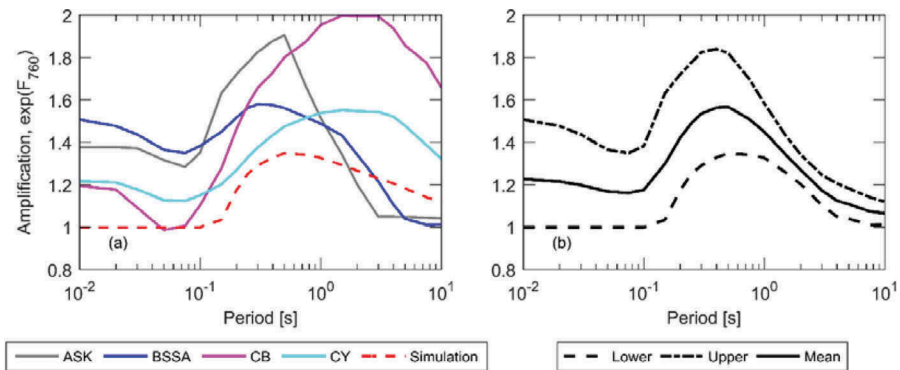


Figure 14. (a) Various amplification factors for a 0.76 km/s condition relative to a hard rock condition (ranging from 1.5 to 2.78 km/s). Amplifications are shown from simulations (Campbell and Boore 2016, hard rock V_S of 2.78 km/s) and four of the NGA West2 GMMs (ASK, BSSA, CB, and CY, hard rock V_S of 1.5 km/s, which is the upper limit of the models). These amplifications were used to develop a mean or “best” estimate and upper/lower bounds as shown in (b).

$$f_1^B = \eta_S + f_1^{erg} + F_{760}^B = f_1 + F_{760}^B \quad (14)$$

where f_1^{erg} is the linear site response from the ergodic GMM used in residuals analysis. Figure 15 shows the residuals derived from both ground motions stations. Both show a strong peak at the fundamental model site period of 3 sec. Figure 16 shows the f_1 values derived from ground motion records and simulations at (a) the PGA and (b) Sa at the structure period of 1.5 sec. The f_1 values estimated from Station 1 tended to be slightly lower than those estimated from Station 2 and from simulations (Figure 16a), but broadly the alternate f_1 values are similar, with mean values generally falling within the 95% confidence interval of one another. Ultimately a weighted average was computed using the f_1 estimates from Stations 1 and 2 and the simulations, with equal weight assigned to each estimate. Although Station 1 has more records than Station 2 (21 vs 9), it is 0.4 km further away. Accordingly, we assigned equal weight to the f_1 estimates from both stations. Upper/lower f_1 values were estimated using the same approach as the Lucas site, with σ_{eff} taken as the standard error of the GM-based f_1 values at all periods.

The nonlinear component of the site term is shown for the site-specific model (derived from simulation) and the ergodic model in Figure 16 for PGA and Sa at the structure period of 1.5 sec. Relative to the ergodic model, the site-specific model has more nonlinearity at short

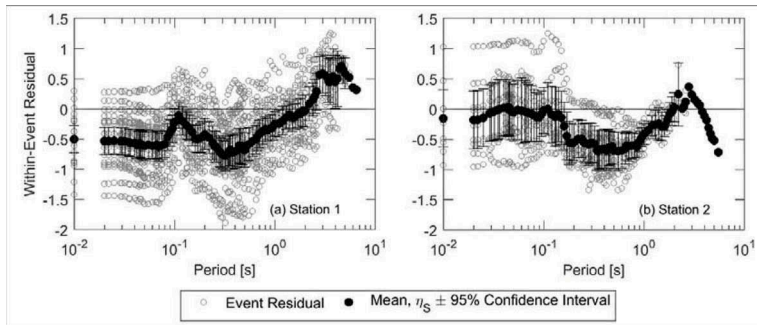


Figure 15. Within-event residuals calculated at (a) Station 1 and (b) Station 2. Also shown are the mean and 95% confidence intervals.

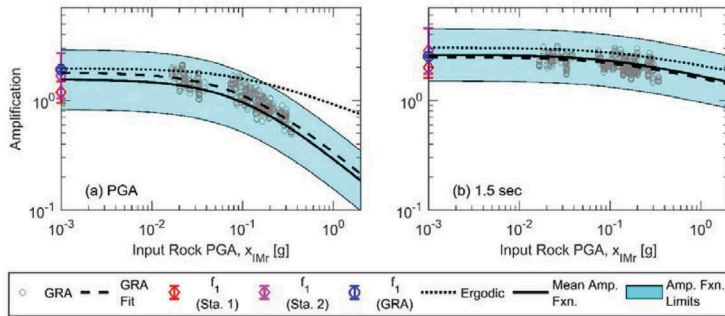


Figure 16. Input/rock PGA versus amplification at the (a) PGA and (b) Sa at 1.5-sec. Note that the linear f_1 parameters calculated from ground motion records at the Stations 1 and 2 and linear GRA are shown. The thick solid black line and shaded region represent the mean and limits of the amplification function used in the analysis, respectively.

periods and about the same nonlinearity at 1.5 sec. Note that the ground motion parameter used in the nonlinear site term applies for the V_{S30}^B condition, and is computed as,

$$\ln(x_{IMr}^B) = \ln(x_{IMr}) - F_{760,IMr}^B \quad (15)$$

where $F_{760,IMr}^B$ is the value of F_{760}^B evaluated for intensity measure IMr (usually PGA).

Because the reference condition for the site term is different from that in GMMs, the site term cannot be added to source and path terms. This can be accommodated by subtracting F_{760}^B in the application of the GMM (Eq. 1). This of course offsets its addition in Eq. (14), but is nonetheless desirable in many cases where the derivation of site response relative to a specific base-of-profile condition is more intuitive.

Figure 17a shows the 2475-year mean uniform hazard spectra derived using ergodic and non-ergodic analysis. Epistemic uncertainties have not been fully considered yet in the derivation of uniform hazard spectra for this site; in particular, the site response uncertainties shown in Figure 16 have not yet been considered. Figure 17b shows the ergodic and non-ergodic 84th percentile deterministic response spectra associated with an **M** 8.1 earthquake on the San Andreas Fault that ruptures the segment nearest the site. Per the building code, the deterministic non-ergodic spectra ultimately controlled the design spectrum at this site. In both cases, the non-ergodic spectra are up to 60% lower than their ergodic counterparts at short periods. At the fundamental-mode structural period (1.5 sec), the ergodic spectra are approximately 30% below the non-ergodic spectra. Conversely, at the site period (3 sec), the non-ergodic deterministic and UHS spectra are approximately equal to or slightly higher than ergodic counterparts, respectively. This increase is due to the fact that the ergodic models tend to under-predict spectral accelerations at the site period (Figure 15). At longer periods, the non-ergodic spectra are slightly below their ergodic counterparts, primarily due to the reduction in the within-event standard deviation.

4.3 Calabrian Dam

The Menta Dam is located in Calabria, Italy, as shown in Figure 18. Unlike the two California sites described above, in this case the ground motion instruments are located directly adjacent to the dam. As a result, the issue of spatial correlation of site terms is not important in this case. The site condition at the instruments and beneath the dam is metamorphic rock (mainly micascists and paragneiss) belonging to Calabrian Complex bedrock. This analysis performed for this site is described in greater detail by Vecchiotti et al. (2019). Challenges (2) and (3) (Section 2.2) were encountered for the PSHA at this site.

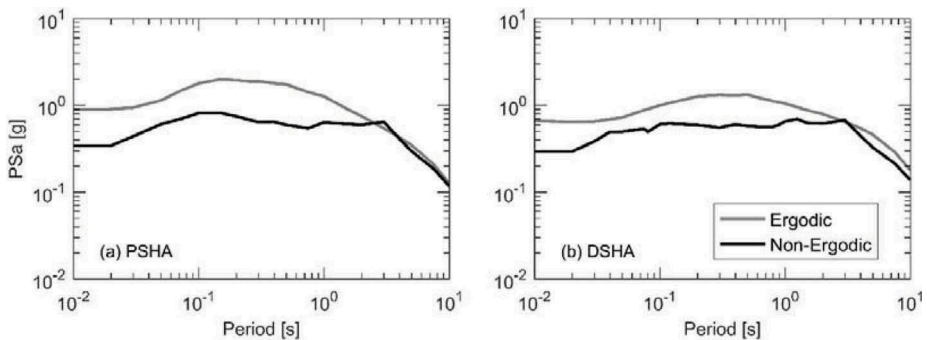


Figure 17. Uniform hazard spectra for a return period of 2475 years (i.e., 2% probability of exceedance in 50 years) derived from ergodic and non-ergodic analysis and (b) 84th percentile deterministic response spectra associated with **M** 8.1 earthquake rupturing the neighboring segment of the San Andreas Fault.

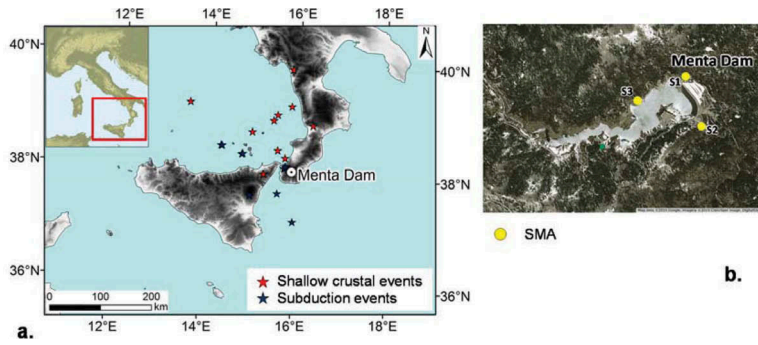


Figure 18. (a) Location of Menta Dam site (southern Italy) and epicenters of events considered in the analysis; (b) SMAs located at the dam site.

No shear wave velocity profile or other dynamic soil properties are available for the site, although H/V spectral ratios have been derived from pre-event noise recorded at the three accelerometers, with the results shown in Figure 19. The H/V spectra show that the site does not exhibit a peaked response indicative of a relative soft layer overlying firmer strata. This suggests a relatively uniform site condition in the metamorphic bedrock. V_{S30} is estimated from surface geology and other factors to be 1000 m/s.

A linear non-ergodic site response model was developed solely based on residuals analysis using data from the three accelerometers. Nonlinearity is assumed to be negligible, which is enforced by setting $f_2=0$. There are data from 20 earthquakes across southern Italy over the approximate time period of 2016-2018, which include both shallow crustal events and subduction slab events associated with the Calabrian subduction zone (e.g. Polonia et al., 2011; Maesano et al., 2017). Ground motions recorded during these events were compiled and processed for the subject site and all other sites for which data could be obtained from open sources (ESM - Engineering Strong-Motion database, and RAN-DPC, Italian Strong Motion Network of Civil Protection Department). As described further by Vecchiotti et al. (2019), these data revealed regional biases in both source and path terms, which were accommodated by adjustments to those terms in the GMMs (Boore et al. 2014 for crustal; Abrahamson et al. 2016 for subduction). Only after making these adjustments were site terms (η_S) derived. As shown in Figure 20, those site terms indicate that the site response is appreciably larger than suggested by the ergodic model for periods lower than 0.4s.

The results in Figure 20 are plotted separately for crustal and subduction sources, which have some differences, although the confidence intervals for each are wide. Given the limited data, and our expectation that linear site response should not be sensitive to event type, we ultimately elected to take an average across all data (emphasizing the crustal data) to develop the η_S used to derive the non-ergodic site term (Eq. 3). The regional adjustments of source

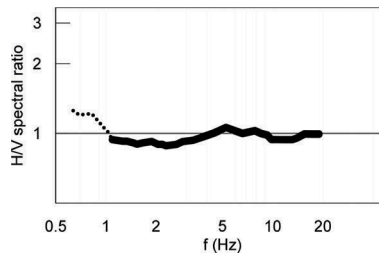


Figure 19. H/V spectral ratios from pre-event noise recorded at the S3 SMA. Similar results obtained for S1-S2

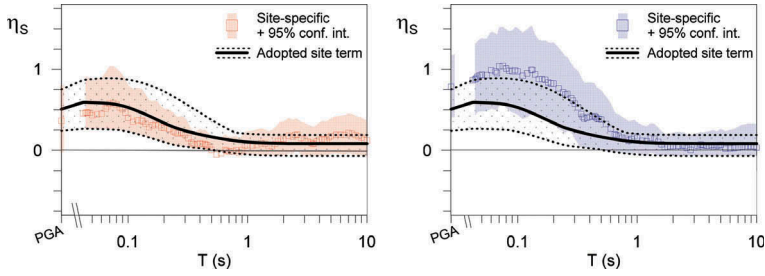


Figure 20. Site terms for the Menta dam site from crustal and subduction recordings. Red plot: crustal fault sources, blue plot: subduction sources.

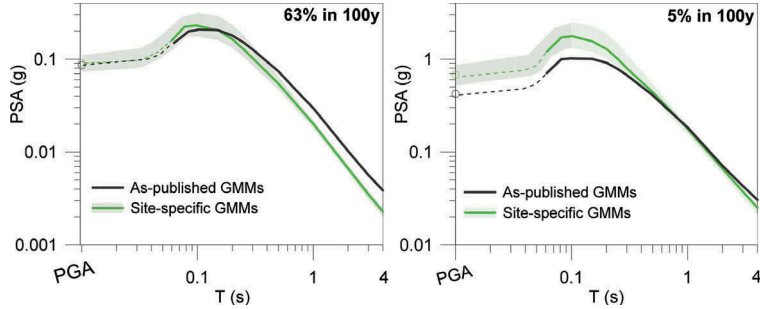


Figure 21. Uniform hazard spectra at Menta dam site for hazard levels of 63% and 5% probability of exceedance in 100 years derived from ergodic and non-ergodic analysis. Range shown for site-specific result is based on range of site amplification considered at the present time, as shown in Figure 20.

and path models in the GMMs were critical for this site; had this not been done the divergence of results in Figure 20 would be much larger and would not represent site response effects.

The results of PSHA for the Menta dam site, which included all the relevant seismic sources for the area (according to Italian Database of Individual Seismogenic Sources and recent studies presented in Tiberti et al. 2017), are plotted as uniform hazard spectra in Figure 21 at two hazard levels, namely 0.63 and 0.05 probability of exceedance in 100 years. The site-specific GMMs emphasize site amplification for periods in the range 0.1-0.4 sec. The uniform hazard spectra from non-ergodic analysis are lower than those from ergodic analysis, due both the change in mean (at periods outside of the range 0.1-0.4 sec) and the reduction of standard deviation. Epistemic uncertainties in the hazard have not been fully considered as of this writing. The range shown in Figure 21 is based on the range of site amplification shown in Figure 20 and some source-related uncertainties.

5 CONCLUSIONS

We have reviewed the non-ergodic site response methodology, documented several challenges that have been encountered in its implementation, and described how those challenges have been addressed in various projects.

The issue of spatial correlation is critical for non-ergodic site response analyses that are informed by ground motion observations. In many cases, the instruments used for the analyses are not located at the sites of interest (as with the Lucas and Sunnyvale sites), requiring judgments to be made about the applicability of the data to the site. Ultimately, as models for the spatial correlation of site response become more fully developed, site terms can be evaluated on a regional basis using Kriging analysis that considers the semi-variance of the data

(shown in Section 3) and its site-dependence (not yet investigated). Such analyses would allow the epistemic uncertainty of the site term to be determined in a way that reflects its proximity to all neighboring observation sites. The current state of knowledge does not allow for this, although preliminary analyses as described in Section 3 are promising. In lieu of such knowledge, correlation has been assumed to be present when site conditions are similar, for example as reflected by similar H/V spectral ratios.

Another issue often faced in the implementation of non-ergodic analyses is consistency of the reference site condition as used in site amplification derived from ground motion data analysis and from simulations. Stewart et al. (2017) describe adjustments that can be made to ensure consistency, which is extended here for cases where the reference site condition is firmer than represented in ergodic models.

Finally, we describe a challenging application of non-ergodic analysis in which geotechnical data was limited and the selected GMMs were biased for application to the study region. As described in Section 4.3, and Vecchietti et al. (2019), the non-ergodic methodology can accommodate such cases, although the epistemic uncertainty on the estimated site terms is relatively large.

REFERENCES

- Abrahamson, N., Gregor, N. & Addo, K. 2016. BC Hydro ground motion prediction equations for subduction earthquakes. *Earthquake Spectra* 32(1): 23–44.
- Afshari, K., Stewart, J.P., 2017. *Implications of California vertical array data for the analysis of site response with 1D geotechnical modeling*, Report to California Geological Survey, Civil & Environmental Engineering Department, UCLA.
- Al Atik, L., 2015. *NGA-East: Ground motion standard deviation models for Central and Eastern North America*, PEER Report No. 2015/09, Pacific Earthquake Engineering Research Center, University of California, Berkeley, CA.
- Ancheta, T.D., Darragh, R.B., Stewart, J.P., Seyhan, E., Silva, W.J., Chiou, B.S.-J., Wooddell, K.E., Graves, R.W., Kottke, A.R., Boore, D.M., Kishida, T., Donahue, J.L., 2014. NGA-West2 database *Earthquake Spectra* 30: 989–1005.
- Atkinson, G. M., 2006. Single-station sigma, *Bull. Seism. Soc. Am.* 96: 446–455.
- Benedikt, G., Pebesma E., Heuvelink, G., 2016. Spatio-Temporal Interpolation using gstat. *The R Journal* 8(1): 204–218.
- Bommer, J. J., 2012. Challenges of building logic trees for probabilistic seismic hazard analysis, *Earthquake Spectra* 28: 1723–1735.
- Bommer, J. J., Abrahamson, N. A., 2006. Why do modern probabilistic seismic hazard analyses lead to increased hazard estimates? *Bull. Seismol. Soc. Am.* 96: 1967–1977.
- Bommer, J. J., Scherbaum, F., 2008. The use and misuse of logic trees in probabilistic seismic hazard analysis, *Earthquake Spectra* 24: 997–1009.
- Bommer, J. J., Coppersmith, K. J., Coppersmith, R. T., Hanson, K. L., Mangongolo, A., Neveling, J., Rathje, E.M., Rodriguez-Marek, A., Scherbaum, F., Shelembe, R., Stafford, P. J., and Strasser, F. O., 2015. A SSHAC Level 3 probabilistic seismic hazard analysis for a new-build nuclear site in South Africa. *Earthquake Spectra* 31: 661–698.
- Boore, D. M., Stewart, J. P., Seyhan, E., and Atkinson, G. M., 2014. NGA-West 2 equations for predicting PGA, PGV, and 5%-damped PSA for shallow crustal earthquakes, *Earthquake Spectra* 30: 1057–1085.
- Campbell, K.W. and Boore, D.M. 2016. Evaluation of Six NEHRP B/C Crustal Amplification Models Proposed for Use in Western North America, *Bull. Seismol. Soc. Am.* 106(2): 673–686
- Cressie, N., 1993, *Statistics for Spatial Data*. Wiley.
- Cressie, N., Wikle C., 2011, *Statistics for Spatio-temporal Data*. Wiley.
- DISS Working Group, 2018. Database of Individual Seismogenic Sources (DISS), Version 3.2.1: A compilation of potential sources for earthquakes larger than M 5.5 in Italy and surrounding areas. <http://diss.rm.ingv.it/diss/>.
- ENGE0. 2017. *Seismic Hazard Analysis Optimization, Revision No. 1*, Lucas Museum of Narrative Art, Los Angeles California, Revised November 21, 2017, Project No. 13604.000.000.
- García-Jerez, A., Piña-Flores, J., Sánchez-Sesma, F. J., Luzón, F., & Pertón, M. 2016. A computer code for forward calculation and inversion of the H/V spectral ratio under the diffuse field assumption. *Computers & Geosciences* 97: 67–78.
- GeoPentech, 2015. *Southwestern United States ground motion characterization SSHAC level 3 – technical report rev. 2*, March 2015.

- Gräler B., Pebesma E., and Heuvelink G., 2016. Spatio-Temporal Interpolation using gstat. *The R Journal* 8(1): 204–218.
- Landwehr, N., Kuehn, N.M., Scheffer, T., Abrahamson, N.A., 2016. A Nonergodic Ground-Motion Model for California with Spatially Varying Coefficients, *Bull. Seism. Soc. Am.* 106: 2574–2583
- Luzi, L., Puglia, R., Russo, E. & ORFEUS WG5. 2016. Engineering Strong Motion Database, version 1.0. Istituto Nazionale di Geofisica e Vulcanologia, Observatories & Research Facilities for European Seismology. <http://esm.mi.ingv.it>
- Maesano, F.E., Tiberti, M.M. & Basili, R. 2017. The Calabrian Arc: three-dimensional modelling of the subduction interface. *Scientific reports* 7(1):8887.
- National Cooperative Highway Research Program, NCHRP, 2012. *Practices and Procedures for Site-Specific Evaluations of Earthquake Ground Motions, Synthesis 428* (N Matasovic and YMA Hashash), Transportation Research Board, Washington D.C.
- National Institute of Standards and Technology, NIST, 2012. *Soil-structure interaction for building structures*, Report No. NIST GCR 12-917-21, U.S. Department of Commerce, Washington D.C.
- Pebesma, E.J., 2004. Multivariable geostatistics in S: the gstat package. *Computers & Geosciences* 30: 683–691.
- Polonia, A., Torelli, L., Mussoni, P., Gasperini, L., Artoni, A., & Klaeschen, D. 2011. The Calabrian Arc subduction complex in the Ionian Sea: Regional architecture, active deformation, and seismic hazard. *Tectonics* 30(5).
- RAN-DPC. Italian Strong Motion Network. Italian Civil Protection Department - Presidency of the Council of Ministers. <http://ran.protezionecivile.it>
- Rathje, E.M., Dawson, C., Padgett, J.E., Pinelli, J.-P., Stanzione, D., Adair, A., Arduino, P., Brandenberg, S.J., Cockeril, T., Esteva, M., Haan, F.L. Jr., Hanlon, M., Kareem, A., Lowes, L., Mock, S., and Mosqueda, G., 2017. DesignSafe: A new cyberinfrastructure for natural hazards engineering. *Natural Hazards Review*: 18.
- Rodriguez-Marek, A., Rathje, E. M., Bommer, J. J., Scherbaum, F., and Stafford, P. J., 2014. Application of single-station sigma and site response characterization in a probabilistic seismic hazard analysis for a new nuclear site, *Bull. Seismol. Soc. Am.* 104: 1601–1619.
- Seyhan, E., Stewart, J. P., Ancheta, T. D., Darragh, R. B., and Graves, R. W., 2014. NGA-West 2 site database, *Earthquake Spectra* 30: 1007–1024.
- Stafford, J. S., Rodriguez-Marek, A., Edwards, B., Kruiver, P. P., and Bommer, J. J. 2017. Scenario dependence of linear site-effect factors for short-period response spectral ordinates. *Bull. Seismol. Soc. Am.* 107(6): 2859–2872.
- Stewart, J.P., Afshari, K., and Hashash, Y. M. A., 2014. *Guidelines for performing hazard-consistent one-dimensional ground response analysis for ground motion prediction*, PEER Report No. 2014/16, Pacific Earthquake Engineering Research Center, UC Berkeley, CA.
- Stewart, J.P., Afshari, K., Goulet, C.A., 2017. Non-ergodic site response in seismic hazard analysis, *Earthquake Spectra* 33: 1385–1414.
- Stewart, J.P. and Stewart, A.F. (1997). *Analysis of soil-structure interaction effects on building response from earthquake strong motion recordings at 58 sites*, Rpt. No. UCB/ERC-97/01, Earthquake Engineering Research Center, University of California, Berkeley, February, 742 pgs.
- Teague, D., Cox, B. R., Bradley, B. A., & Wotherspoon, L. M., 2017. Development of deep shear wave velocity profiles with estimates of uncertainty in the complex interbedded geology of Christchurch, New Zealand. *Earthquake Spectra* 34(2): 639–672
- Teague, D. P., Cox, B. R., & Rathje, E. M., 2018. Measured vs. predicted site response at the Garner Valley downhole array considering shear wave velocity uncertainty from borehole and surface wave methods. *Soil Dyn. and Earthquake Eng.* 113: 339–355.
- Tiberti M.M., Vannoli P., Fracassi U., Burrato P., Kastelic V., Valensise G. 2017. Understanding seismogenic processes in the Southern Calabrian Arc: a geodynamic perspective. *Italian Journal of Geosciences* 136 (3): 365–388
- Wentworth, C.M., Jachens, R.C., Williams, R.A., Tinsley, J.C., and Hanson, R.T., 2015. *Physical Sub-division and Description of the Water-Bearing Sediments of the Santa Clara Valley, California*, United States Geological Survey, Scientific Investigations Report 2015-5017.
- Vecchiotti, A., Stewart, J.P., Cecconi, M., Pane, V. & Russo, G. 2019. Non-ergodic site response model based on local recordings for Menta Dam site. *Proc. 7th International Conference on Earthquake Geotechnical Engineering, Rome, 17-20 June 2019.*